

## Article

# One-Step Multi-Doping Process for Producing Effective Zinc Oxide Nanofibers to Remove Industrial Pollutants Using Sunlight

Osama Saber <sup>1,2,\*</sup> , Nagih M. Shaalan <sup>1,3</sup> , Faheem Ahmed <sup>1</sup> , Shalendra Kumar <sup>1,4</sup>  and Adil Alshoaibi <sup>1</sup>

<sup>1</sup> Department of Physics, College of Science, King Faisal University, P.O. Box 400, Al-Ahsa 31982, Saudi Arabia; nmohammed@kfu.edu.sa (N.M.S.); fahmed@kfu.edu.sa (F.A.); sjagdish@kfu.edu.sa (S.K.); aalshoaibi@kfu.edu.sa (A.A.)

<sup>2</sup> Egyptian Petroleum Research Institute, Nasr City, P.O. Box 11727, Cairo 11765, Egypt

<sup>3</sup> Physics Department, Faculty of Science, Assiut University, Assiut 71516, Egypt

<sup>4</sup> Department of Physics, School of Engineering, University of Petroleum & Energy Studies, Dehradun 248007, India

\* Correspondence: osmohamed@kfu.edu.sa

**Abstract:** Doping processes for optical materials are one of the driving forces for developing efficient and clean technologies for decontamination of aquatic effluents through lowering their band gap energy to become effective in sunlight. The current study has used a non-conventional technique for doping zinc oxide by multi metals, non-metals and organic dyes through a one-step process. In this trend, Zn-Al nanolayered structures have been used as hosts for building host–guest interactions. Organic dyes that have inorganic species of iron, nitrogen and sulfur have been used as guests in the intercalation reactions of Zn-Al layered double hydroxides. By intercalating green dyes, organic–inorganic nanohybrids were formed as nanolayered structures with expanding interlayered spacing to 2.1 nm. By changing the concentration of green dyes and thermal treatment, series of nanofibers and nanoplates of zinc oxides were formed and doped by aluminum, iron and sulfur in addition to colored species. The optical properties of the multi-doped zinc oxide indicated that it became suitable for solar applications because its band gap energy decreased from 3.30 eV to 2.80 eV. The experimental and kinetic results of the multi-doped zinc oxide concluded that the colored pollutants were effectively removed during 50 min of sunlight irradiation.

**Keywords:** host-guest interaction; lowering band gap energy; nanofibers; nanohybrids; multi-doped oxides; photocatalytic degradation of industrial pollutants in sunlight



**Citation:** Saber, O.; Shaalan, N.M.; Ahmed, F.; Kumar, S.; Alshoaibi, A. One-Step Multi-Doping Process for Producing Effective Zinc Oxide Nanofibers to Remove Industrial Pollutants Using Sunlight. *Crystals* **2021**, *11*, 1268. <https://doi.org/10.3390/cryst11101268>

Academic Editors: Assem Barakat and Alexander S. Novikov

Received: 24 September 2021

Accepted: 15 October 2021

Published: 19 October 2021

**Publisher's Note:** MDPI stays neutral with regard to jurisdictional claims in published maps and institutional affiliations.



**Copyright:** © 2021 by the authors. Licensee MDPI, Basel, Switzerland. This article is an open access article distributed under the terms and conditions of the Creative Commons Attribution (CC BY) license (<https://creativecommons.org/licenses/by/4.0/>).

## 1. Introduction

A sustainable society is currently a target for scientific communities. It aims at the remediation of ecosystems and biomes through developing efficient and clean technologies for decontamination of aquatic effluents. In this trend, heterogeneous photocatalysis is known as an efficient and clean technique for decontamination of aquatic effluents, since it uses light energy as a driving force for full conversion of organic compounds to carbon dioxide and water. However, the photo-active materials used in these processes still have weak points that limit the potential capability of using this technique on a large scale, such as a low visible light absorption and high recombination of photo-generated charges [1]. Recently, using sunlight and semiconductors, photocatalytic degradation of colored pollutants appears to be a good solution for cleaning water from dyes [2,3].

Dindar and Icli [4] had studied the photocatalytic activity of different semiconductors such as zinc oxide, iron oxides and titanium dioxide through degradation of phenol under visible light. They indicated that zinc oxide showed higher efficiency than the other semiconductors for phenol degradation in presence of sunlight. This indication was confirmed through the advanced oxidation of pulp mill bleaching wastewater using zinc oxide and

titanium oxide semiconductors. Zinc oxide was found to be more efficient than titanium oxide [5,6]. In many countries such as Saudi Arabia, where ample sunlight is available, a photocatalysis technique using sunlight will be preferable and cheap because solar energy containing 4% ultraviolet radiation and 43% visible light is inexhaustible and free [7–9]. However, the large band gap energy of 3.37 eV is the main disadvantage of ZnO that absorbs wavelengths below 400 nm for excitation. Another drawback of zinc oxide is that photo-generated electron–hole pairs recombine again within nanoseconds leading to low photocatalytic activity [10]. Also, Wang et al. [11] and Zhou et al. [12] confirmed that the fast recombination rate of the photo-generated electron–hole pairs of zinc oxide and the low quantum yield in the photocatalytic processes in aqueous solutions obstruct commercialization of the photocatalytic degradation process. Therefore, it is a great challenge and necessary to enhance the visible-light activity of zinc oxide through shifting its absorption threshold from the region of UV light to the region of visible-light. In addition, a reduction of the recombination rate of photo-generated electron–hole pair can induce an effective photocatalyst in sunlight. In order to solve the problems of zinc oxide, different products and several techniques were applied and reported. Doping processes with transition elements, morphological changes, nanomaterials formation [13], combining with carbon nanotubes [14] and introducing surface defects [15] were proposed as suitable solutions for preventing the drawbacks of zinc oxide photocatalysts. In this trend, nanoparticles [16], nanorods [17], nanotubes [18], and nanowires [19] were prepared to increase the optical properties and activity of zinc oxide. Recently, Diguna, et al. [20] concluded that the optical and photodetection properties of ZnO improved through preparing its nanoparticles from Zn Dross.

Doping of zinc oxide with transition elements is one of the best solutions for solving the problems of ZnO to act as effective photocatalysts [21–25]. Strong scientific efforts have been achieved to attain such a goal during recent years by synthesizing nanomaterials or introducing intrinsic and extrinsic dopants to ZnO structure to improve its optical properties through increasing the carrier concentration in the photocatalysis process. Intrinsic dopants can be produced through lattice defects such as oxygen vacancies or zinc interstitials. The other way is the introduction of trivalent atoms inside a zinc lattice to act as extrinsic dopants.

Sheriff et al. [26] indicated that the addition of sulfur inside ZnO could improve the charge separation by suppressing the electrons and holes recombination process. Also, the addition of Al and Ag inside ZnO films was studied by Adeel et al. for the photocatalytic degradation of colored pollutants under UV irradiation exhibiting high photocatalytic degradation of rhodamine blue and methylene blue [27]. N-doping process for ZnO nanospheres was achieved by Atul et al. through micro-emulsion method to produce very active photocatalysts in the visible light [28]. In addition, several studies were carried out for producing transparent thin films of ZnO and the doped ZnO with Al and Fe to be useful for solar cell and photocatalytic applications [29–34].

Our previous research [7] concluded that the Al-doping process has positive effect for improving photocatalytic activity of ZnO. Thus, the current research aims to improve the photocatalytic activity of ZnO structure by multi-doping process through an unconventional technique. In the conventional methods [35], one or two elements are used as a dopants for ZnO and this is achieved through multi-steps. However, it is difficult to obtain a homogenous distribution for both dopants in the matrix of ZnO in this way. Therefore, many researchers avoid using multi dopants for ZnO.

The current study has used an unusual approach for inserting Al, Fe and sulfur in addition to green dyes inside ZnO structure. It was achieved through host–guest interaction. The host was produced by inserting Al with Zn inside the nanolayers of layered double hydroxides. Layered double hydroxides (LDH) are of specific importance because they have nanolayered structures containing various kinds of metals and different species of non-metal with an order arrangement in their layers [36–38]. In this way, cationic nanolayers containing Zn and Al were formed having positive charges. Green dyes were

used as guests. These guests which are anion and contain iron, nitrogen and sulfur as inorganic elements in addition to organic species have been used as spacers between the nanolayers. By host–guest interaction, organic–inorganic nanohybrids were formed in ordered arrangements through nanolayered structures. This strategy allows combining different metals and non-metals with zinc oxide structure in special arrangements in the nano scale producing nanocomposites and a nanohybrid based on zinc oxide structure, aiming to increase its ability for suppressing charge recombination and narrowing its band gap energy [39].

In the current study, a series of nanohybrids which contain Zn-Al-dyes have been prepared using host–guest interactions. The structural properties of the prepared materials were measured by different techniques. The optical parameters and band gap energy were studied through a UV/VIS/NIR spectrophotometer through the diffuse reflectance technique. The photocatalytic activity of the doped samples was measured by photocatalytic decomposition of colored pollutants. In addition, a kinetic study of photocatalytic reactions was studied for all the prepared materials.

## 2. Materials and Methods

Urea, aluminum nitrate  $\text{Al}(\text{NO}_3)_3 \cdot 9\text{H}_2\text{O}$  and zinc nitrate  $\text{Zn}(\text{NO}_3)_2 \cdot 9\text{H}_2\text{O}$  were acquired from Sigma Aldrich (Sigma Aldrich, St. Louis, MO, USA). Series of nanohybrids were prepared through host–guest interaction. Zinc nitrate and aluminum nitrate were used as sources for building the host. A green dye (Naphthol Green B) was used as a guest. To prepare the first nanohybrid, zinc and aluminum nitrates were dissolved in one liter of deionized water for producing an aqueous solution (0.07 M). The molar ratio between zinc and aluminum was 3:1. A 0.5 mol of urea was added to the aqueous solution to act as a precipitant and pH-controller. The prepared solution was mixed with 1 g of Naphthol Green B under vigorous stirring. The aqueous solution was heated at 70 °C until PH = 9. The green product was washed and filtered by deionized water several times. This sample was coded by ZONH1. By decreasing the content of green dyes to become 0.5 g and 0.1 g, two other nanohybrids were prepared and coded by ZONH2 and ZONH3; respectively. The fourth sample was prepared without green dyes for comparison. It was called AZO.

The prepared samples were thermally treated at 500 °C for 6 h in presence of air. The rate of heating was 10 °C/min. The color of the samples changed from green color to yellow color. The codes of the samples became ZONH1-500, ZONH2-500 and ZONH3-500. To study the effect of temperature, the sample ZONH1 was calcined at 1200 °C.

One of the main tools widely used for determining the crystal structure of the prepared compounds is powder X-ray diffraction. The results of X-ray diffraction were recorded by Bruker-AXS, Karlsruhe, Germany with Cu-K radiation ( $\lambda = 0.154 \text{ nm}$ ). Energy-dispersive X-ray spectroscopy is an analytical technique used to probe the composition of solid materials. Energy-dispersive X-ray spectroscopy measurements were carried out using an Electron Probe Micro analyser JED 2300. Fourier transform infrared spectroscopy (FTIR) is one of the molecular vibrational spectroscopic techniques for both quantitative and qualitative analysis. FTIR is used to investigate the structural bonding and chemical properties of compounds through recording on a Perkin Elmer Spectrum 400 over the wave number range 425–4000  $\text{cm}^{-1}$ . Thermal gravimetric analysis (TGA) was carried out in a TA thermogravimetric analyzer (series Q500, TA Company, New Castle, PA, USA) under  $\text{N}_2$  atmosphere to a maximum temperature of 800 °C. The morphology and size of the synthesized product were measured by scanning electron microscopy (SEM) with a model JSM-6330F, 15 kV/12  $\mu\text{A}$ , JEOL Company, Tokyo, Japan. The transmission electron microscopy (TEM) was carried out at room temperature JEM 2100F with acceleration voltage of 200 kV. By a diffuse reflectance technique, a UV/VIS/NIR Shimadzu 3600 spectrophotometer attached with an integrating sphere ISR-603 (Shimadzu, Columbia, MD, USA) measured the optical properties of the solid materials. In order to determine the concentration of liquid samples, the same UV-Vis spectrophotometer was used to measure the absorbance of the colored samples.

By photocatalytic degradation of Naphthol Green B (NGB), the photo-activity of the prepared samples was determined in sunlight. In the current research, the aqueous solution of NGB was prepared to have a low concentration  $4 \times 10^{-4}$  M. Then, it was mixed with 0.1 g of the prepared sample to be well-dispersed in the solution. When the initial concentration of dye is low, the intensity of the measured spectrum of the dye is proportional to the concentration of the dye according to the law of Beer–Lambert. The mixture was irradiated by sunlight. The irradiation area is  $10 \text{ cm}^2$ . Every 10 min of radiation in sunlight, a certain amount of the dye was extracted to measure its concentration by using UV-Vis spectrophotometer. By comparing the calculated area of the typical peak of Naphthol Green B at  $714 \pm 10 \text{ nm}$  before and after irradiation, the effect of the photocatalyst on the concentration of the green dye is determined. The photocatalysis processes of the current research were carried out in the sunlight of Saudi Arabia in the summer season (July) from the time 9:30 a.m. to 10:30 a.m.

It is known that sunlight consists of three major parts: (1) visible light, with wavelengths 400–800 nm, (2) ultraviolet light, with wavelengths shorter than 400 nm, and (3) infrared radiation, with wavelengths longer than 800 nm. In Saudi Arabia, there is a plenty amount of sunlight. The spectrum of solar UV light is from 290 nm to 390 nm. This spectrum is divided into two parts; the wavelengths covering 320 to 390 nm are referred to as UV-A and 290 to 320 nm as UV-B [40]. In the eastern region of Saudi Arabia, the maximum recorded hourly mean irradiance UV radiation was  $28 \text{ W/m}^2$  in July.

### 3. Results

#### 3.1. Host–Guest Interactions for Building Nanohybrids

Layered double hydroxides have been used for doping zinc oxides with aluminum through nanolayered structures. The characteristic peaks of the sample AZO are observed in Figure 1a.

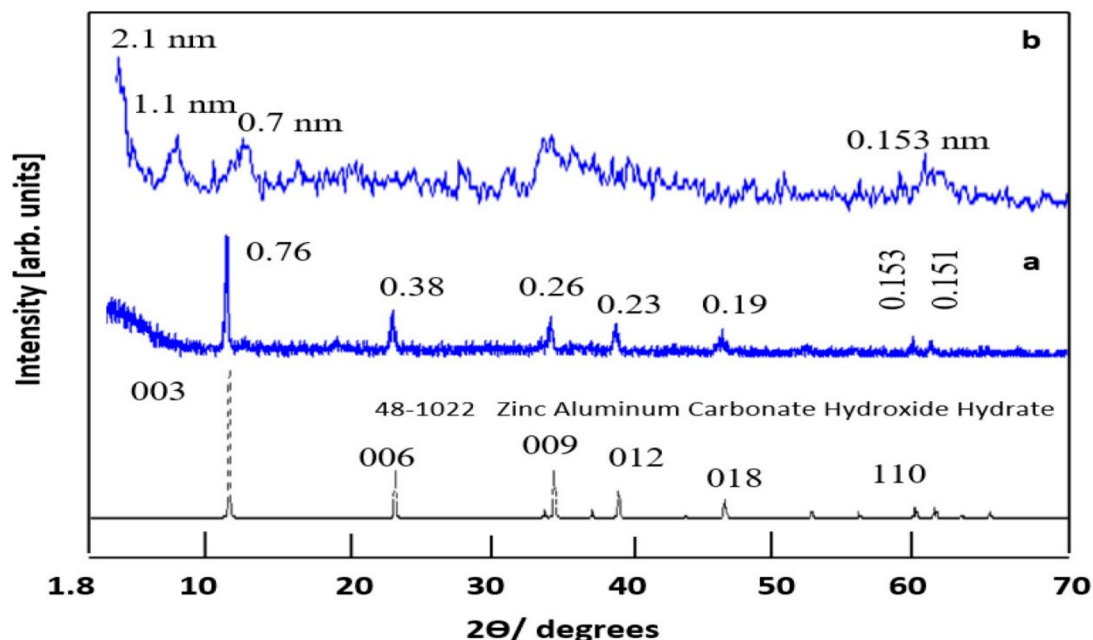


Figure 1. X-ray diffraction (XRD) patterns of (a) AZO and (b) ZONH1.

The powder X-ray diffraction pattern of AZO agrees with the data of hydroxalite-like materials (JCPDS file No. 37-629) and fits entirely to the layered structure of Zn–Al LDH (JCPDS file No. 48-1022). The symmetric and sharp reflections are observed for the basal (003), (006) and (009) planes. Also, the asymmetric reflections are detected for non-basal (012), and (018) planes as shown in Figure 1a. The successive arrangements among the basal planes, i.e.,  $d_{(003)} = 2 \times d_{(006)} = 3 \times d_{(009)}$  for AZO, showed highly packed stacks of

brucite-like layers. The lattice parameters ( $a, c$ ) of AZO could be evaluated by XRD data. The lattice parameter ' $a$ ' could be calculated as two times the spacing for plane (110), i.e., 0.306 nm. It equals the average cation–cation distance within the brucite-like layer. The value ' $c$ ' corresponds to the summation of both the thickness of the brucite-like layer and the interlayer distance. It is commonly calculated as three times the spacing for plane (003), i.e., 2.28 nm. This value ' $c$ ' agrees with that reported for natural and synthetic hydrotalcite, 2.283 nm. The main peak of AZO was observed at  $2\theta = 11.6^\circ$  corresponding with the d-spacing interlamellar value  $d_{(003)}$  of Zn-Al LDH 0.76 nm as shown in Figure 1a. This value depends on the size of the interlayered anion in addition to the thickness of the brucite-like layers (0.48 nm).

By intercalating Naphthol Green B among the nanolayers of the sample AZO, new nanohybrid was produced through host-guest interaction. Figure 1b showed the XRD pattern of ZONH1. The original main peaks (0.76 nm and 0.38 nm) that belong to Zn-Al LDH (AZO) disappeared. In the same time, new peaks were observed at lower  $2\theta$  (2.1 nm, 1.1 nm and 0.7 nm) confirming formation of organic–inorganic nanohybrid. It means that the two-dimensional layers of Zn-Al confines the molecules of green dye instead of the inorganic anions. The interlayered spacing of the nanolayered structures increased and expanded depending on the thickness of the organic molecules. By comparing with the nanolayered structure of the LDH, the interlayered spacing of ZONH1 expanded from 0.76 nm to 2.1 nm after intercalation reaction with Naphthol Green B. Also, the order arrangement of the layered structures was observed by successive reflections of the basal planes, i.e.,  $2.1 \text{ nm} = 2 \times 1.1 \text{ nm} = 3 \times 0.7 \text{ nm}$ . In the same time, the lattice parameter ' $a$ ' did not change (0.308 nm). However, the value ' $c$ ' increased to be 4.2 nm after the intercalation of Naphthol Green B in place of carbonates ions (2.28 nm). It confirms that the intercalation of Naphthol Green B was completed and the organic–inorganic nanohybrid was formed.

Thermal measurements were used in order to determine and compare the thermal behavior of the interlayered species inside the prepared nanohybrid with that in AZO LDH. The thermal behavior of both AZO and the nanohybrid was evaluated by thermogravimetric analysis (TGA) as shown in Figure 2. The TG curves showed that the thermal degradation of the interlayered species occurred with different rates of weight losses in several steps according to the nature of the interlayer anions.

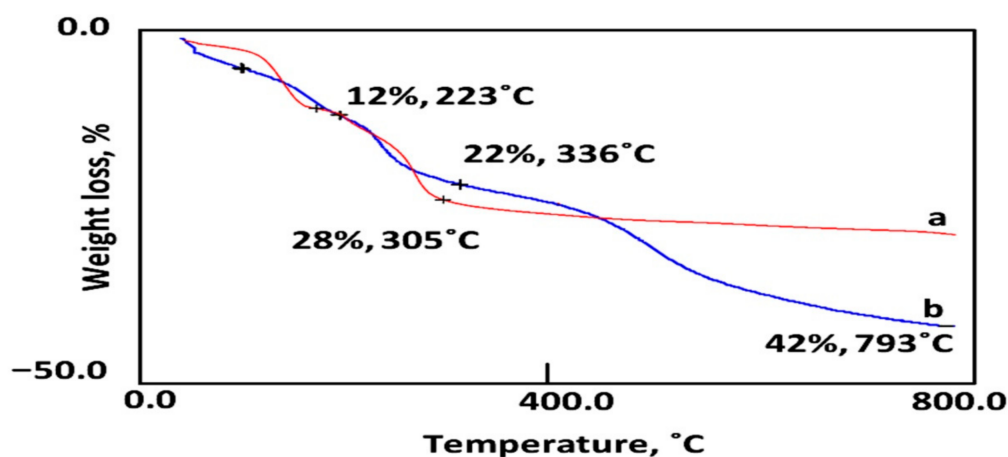


Figure 2. Thermogravimetric analysis of (a) AZO and (b) ZONH1.

In the case of the sample AZO, the total weight loss was 28 wt.% and occurred mainly in two steps as shown in Figure 2a. The TG curve showed that the first step is due to the removal of surface and intercalated water of LDH and their weight losses were 12 wt.%. The decomposition of carbonate anions and the dehydroxylation of layers were happened in the second step by losing 16 wt.% at 305 °C.

After intercalation reactions, the TG curve of the nanohybrid ZONH1 showed that it has three weight losses. 12 wt.% of water was lost in the first stage at 223 °C. By continuing

heating above 223 °C, 30 wt.% of the nanohybrid was lost through two stages. 10 wt.% was removed at 336 °C and 20 wt.% was lost at 792 °C.

By comparing with the AZO LDH, the total weight loss of the nanohybrid ZONH1 increased from 28 wt.% to 42 wt.%. In addition, the degradation temperature of the interlayered species shifted to higher temperature after intercalating Naphthol Green B. The temperature of decomposition processes of LDH was continued up to 305 °C and in the case of the nanohybrid, it was 793 °C. According to the thermal analysis results, a complete formation for the nanohybrid was achieved by intercalating 30 wt.% of Naphthol Green B inside the interlayered spacing of the Al/Zn nanolayered structures.

The nature and symmetry of the interlayer anions of AZO and ZONH1 were identified by FTIR. FTIR spectra of AZO and ZONH1 are displayed in Figure 3.

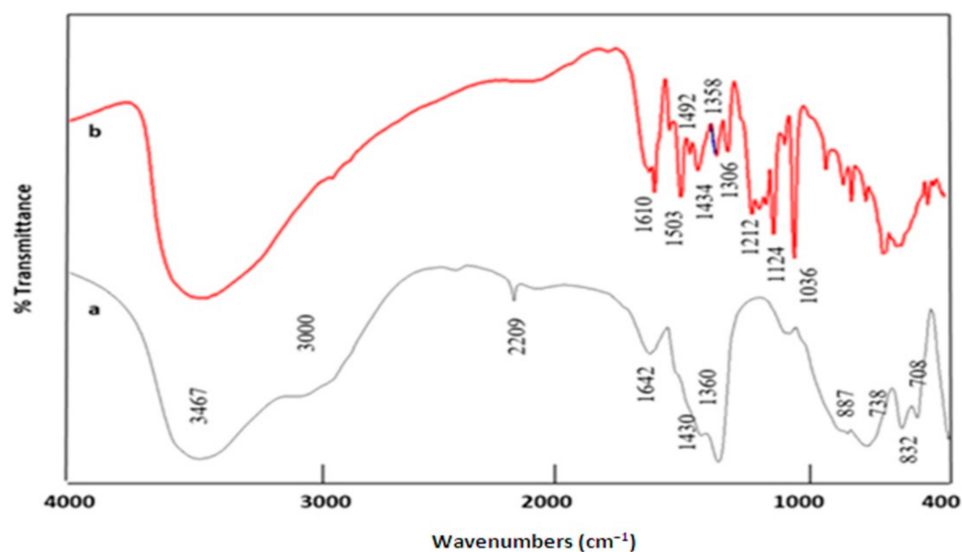


Figure 3. Fourier transform infrared spectra of (a) AZO and (b) ZONH1.

The presence of hydroxyl groups of the nanolayers of AZO was confirmed by a broad absorption in the range of 3400–3600  $\text{cm}^{-1}$ . Figure 3a showed stretching mode of OH band for AZO LDH at 3467  $\text{cm}^{-1}$  noting that the hydrogen bonds caused the extreme broadness of the OH band in addition to the clear shoulder peaks at 3000  $\text{cm}^{-1}$ . Also, these shoulder peaks are due to the O–H stretching mode of interlayer water molecules, hydrogen-bonded to interlayer carbonate anions [40,41]. The band observed at 1642  $\text{cm}^{-1}$  is liable of the bending mode band of water molecules [38,42]. FTIR results indicated that the AZO LDH has two types of interlayered anions. Carbonate anions were observed by two bands at 1430  $\text{cm}^{-1}$  and 1360  $\text{cm}^{-1}$  that are due to the vibrational mode ( $\nu_3$ ) of carbonate [38,41]. Also, the vibrational mode ( $\nu_1$ ) of carbonate was observed as a weak band around 1081  $\text{cm}^{-1}$ . In addition, the sharp bands at 832  $\text{cm}^{-1}$  and 887  $\text{cm}^{-1}$  are ascribed to the vibrational mode ( $\nu_2$ ) of carbonate anions. The bands at 738  $\text{cm}^{-1}$  and 708  $\text{cm}^{-1}$  are due to the vibrational mode ( $\nu_4$ ) of carbonate anions [38,41]. Cyanate anions ( $\text{NCO}^-$ ) are demonstrated by a clear band in the region 2230–2105  $\text{cm}^{-1}$  which is due to the vibrational mode ( $\nu_1$ ) of cyanate as shown in Figure 3a [41,42].

The FTIR spectrum of ZONH1 is shown in Figure 3b and confirmed transformation of AZO LDH to organic–inorganic nanohybrid after its intercalation reaction with Naphthol Green B. Figure 3b shows that ZONH1 has the main peaks of LDH (HO–Zn–Al–OH) with absence of the peaks corresponding to carbonate and cyanate anions and appearing the characteristic peaks of the organic species. It shows peaks at 2950–2800  $\text{cm}^{-1}$  indicating the  $\gamma$ -mode for C–H bonds. Also, the  $\gamma$ -mode for carbonyl group C=O was observed at 1610  $\text{cm}^{-1}$ . In addition, the presence of peaks at 1504  $\text{cm}^{-1}$ , 1492  $\text{cm}^{-1}$  and 1434  $\text{cm}^{-1}$  that are due to the  $\gamma$ -mode of double bonds C=C confirmed existence of the aromatic rings. The  $\delta$ -mode for methyl group ( $-\text{CH}_3$ ) was observed at 1358  $\text{cm}^{-1}$ . The  $\gamma$ -mode for R-SO<sub>2</sub>-OH

was detected at  $1306\text{ cm}^{-1}$ . Figure 3b shows a peak at  $1212\text{ cm}^{-1}$  confirming the presence of Ar-O-CH<sub>3</sub>. The sulphonate group was detected by observing two peaks at  $1124\text{ cm}^{-1}$  and  $1036\text{ cm}^{-1}$  [43,44]. The lattice vibration modes of ZONH1 were observed by peaks at the low frequency region such as the Al-OH translation vibrations at  $790\text{ cm}^{-1}$  and  $554\text{ cm}^{-1}$  and for the Zn-OH at  $613\text{ cm}^{-1}$  [45].

The morphology of the nanohybrid particles synthesized with green dyes is similar to that of the conventional LDH. As shown in Figure 4, the TEM images show plate-like morphology for the nanohybrid. Their sheets are aggregated together because of the hydrophobic behavior of organic species. Also, Figure 4 reveals that the dimensions of the plates are in the order of a few micrometers in width and the thickness is in the nano scale.

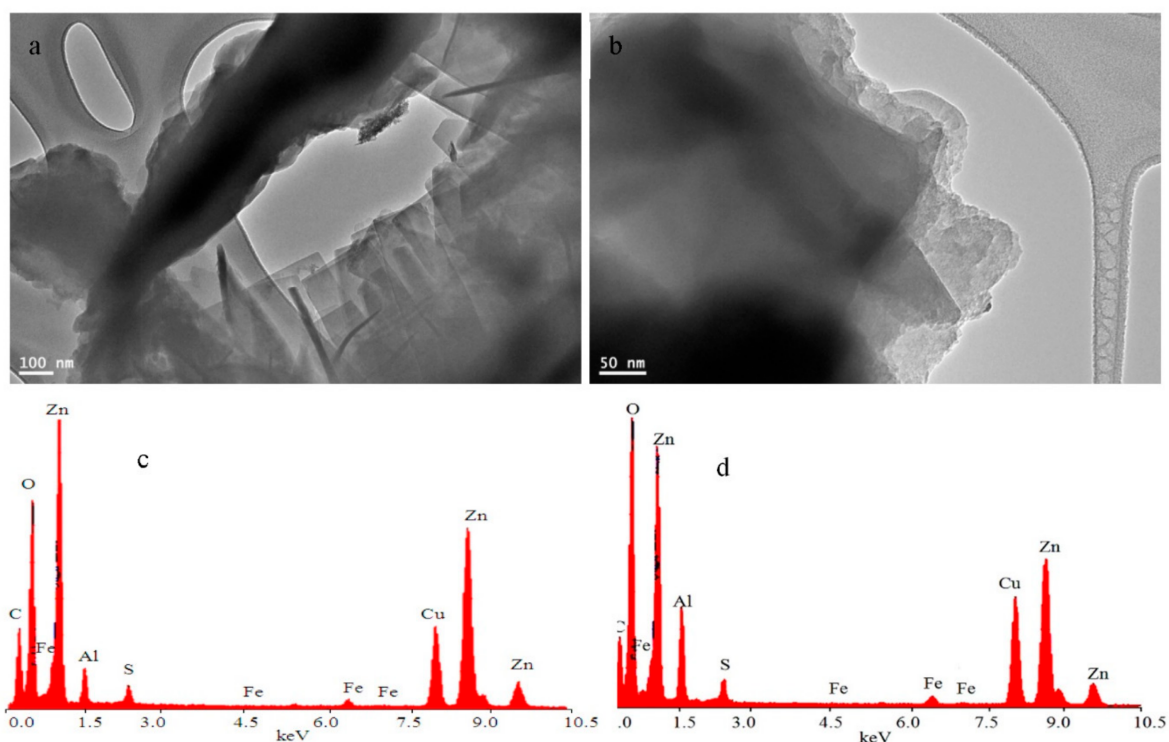


**Figure 4.** Transmission electron microscopy (TEM) images (a,b) and energy-dispersive X-ray (EDX) spectra (c,d) of the nanohybrid ZONH1.

### 3.2. Multi-Doping Process of Zinc Oxide

Through hydrothermal treatment of the prepared nanohybrid at  $500\text{ }^{\circ}\text{C}$  and  $1200\text{ }^{\circ}\text{C}$ , the powder XRD patterns for the calcined nanohybrids ZONH1-500 and ZONH1-1200 are shown in Figure 5. It can be seen from Figure 5a, all the diffracted lines of the calcined nanohybrid at  $500\text{ }^{\circ}\text{C}$  are matching with the peaks of ZnO corresponding to the JCPDS Card No. 79-205. The reflections by various crystal planes agreeing with diffraction from different planes are equivalent to the hexagonal close packed structure of zinc oxide. The peaks broadness of ZONH1-500 is probably due to the nano-size effect.

When compared with the XRD pattern of the standard ZnO, the pattern of ZONH1-500 is clearly seen to be broad and the peak intensity decreases with the hybridization with organic species. In addition, there is no new peak observed in this pattern for the organic species. This indicates that disordering of the crystals of ZnO sample is supported by doping with the inorganic and organic species which produced from the decomposition of organic species. Decomposition reactions of the organic species are expected to occur at  $500\text{ }^{\circ}\text{C}$ , producing ZnO with low crystallinity. The low crystallinity may be due to expansion of crystalline planes in ZnO structure because of a possible slight intercalation of organic species in the ZnO crystals. From the XRD data and using the Debye–Scherer

equation, the crystal size could be estimated. The mean crystallite sizes are shown in Table 1. It was calculated to be  $8 \pm 0.1$  nm.

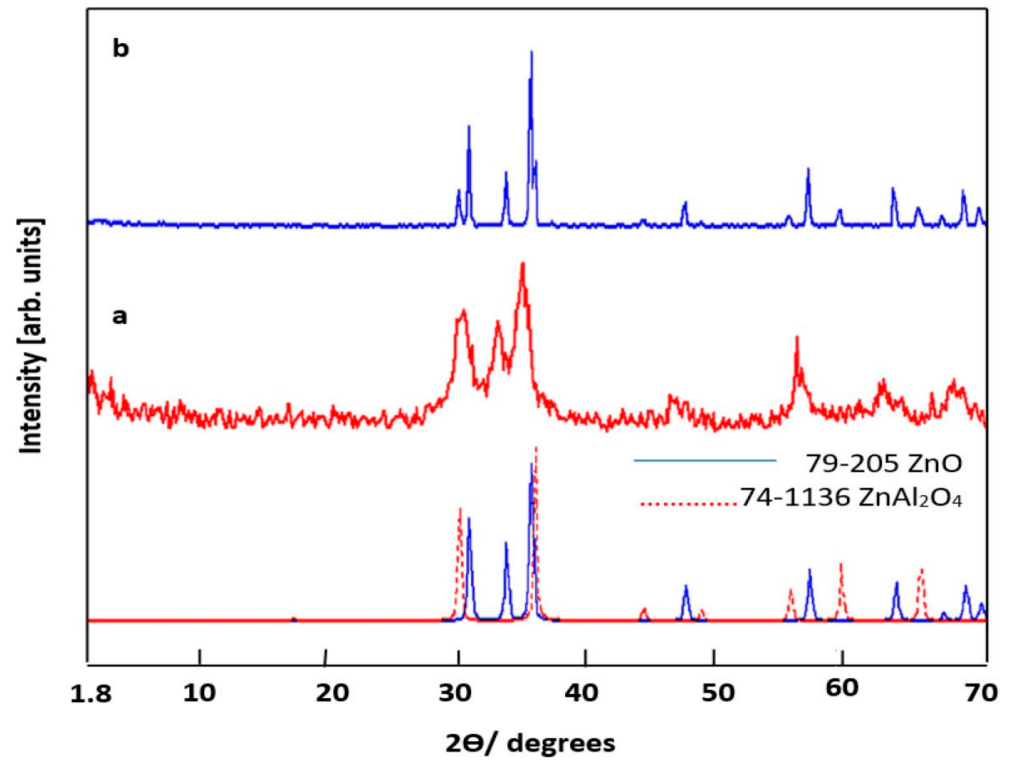


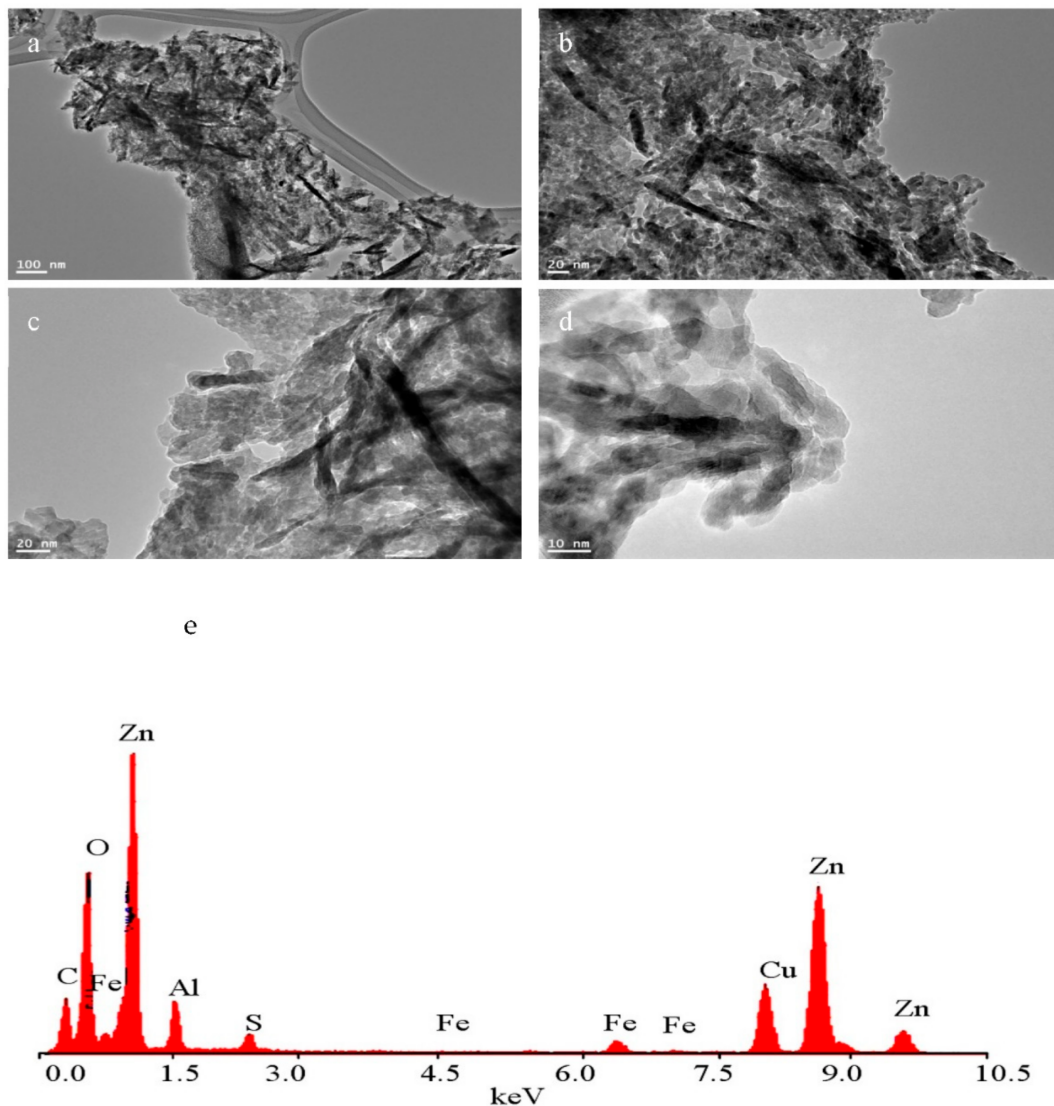
Figure 5. X-ray diffraction patterns of: (a) ZONH1-500, (b) ZONH1-1200.

Table 1. Average crystallite sizes calculated from X-ray results ZONH1-500 and ZONH1-1200.

Sample	(2θ)	Area	Cry. Size (nm)	Av. Size (nm)
ZONH1-500	$31.7 \pm 0.1$	$127 \pm 0.1$	$7.8 \pm 0.1$	$8 \pm 0.1$
	$34.4 \pm 0.1$	$85 \pm 0.1$	$8.3 \pm 0.1$	
	$36.2 \pm 0.1$	$189 \pm 0.1$	$7.8 \pm 0.1$	
ZONH1-1200	$31.7 \pm 0.1$	$94 \pm 0.1$	$132 \pm 0.1$	$125 \pm 0.1$
	$34.4 \pm 0.1$	$69 \pm 0.1$	$123 \pm 0.1$	
	$36.2 \pm 0.1$	$171 \pm 0.1$	$120 \pm 0.1$	

The size of the ZnO crystals suggests that the dopant atoms can combine with the ZnO structure in two ways; in interstice between zinc and oxygen atoms or in substitutional site instead of zinc atom. According to the reduction of the size to be 8 nm by our technique, we can expect that the combination process occurs through substitution because the addition of dopants should shrink the lattice appreciably. Note that the ionic radius of aluminum (0.53 Å) is smaller than that of zinc (0.60 Å), and is predicted by Vegard's law [46]. Also, the preparation technique confirms this speculation as shown later in the discussion section.

In order to support the results of X-ray diffraction, transmission electron microscope was used to determine the crystallite sizes. TEM images showed that the nanolayers of the nanohybrid transformed to nanoparticles. At the same time, the assembling of nanoparticles to be nanofibers was also observed. Figure 6 depicts TEM images of the calcined nanohybrid ZONH1-500 indicating that it has nanoparticles-assembled nanofibers. It is clearly seen from Figure 6c,d that the sample is dominated by nanofibers with lengths of hundreds of nanometer and diameters ranging from 5 to 15 nm. The detailed high-magnification image, shown in Figure 6d, reveals that the surface of the nanofibers is microscopically rough and the rough surface consists of nanoparticles with the particle size less than 10 nm.



**Figure 6.** TEM images (a–d) and EDX spectrum (e) of the nanohybrid ZONH1-500.

The EDX spectrum of the sample ZONH1-500 confirmed presence of iron and sulfur (Fe and S) which belong to decomposition of naphthol green B in addition to zinc and aluminum as shown in Figure 6e. This means that the produced zinc oxide from the decomposition of naphthol green B contains Fe, S and Al as dopants in the matrix of ZnO.

The XRD pattern of the annealed nanohybrid ZONH1-1200 is shown in Figure 5b. All the obtained diffraction lines of ZONH1-1200 were mainly identified as a wurtzite ZnO crystal. However, there is growth for new phase of  $\text{ZnAl}_2\text{O}_4$  with randomly oriented polycrystalline. The percentage of  $\text{ZnAl}_2\text{O}_4$  was 33%. These results indicated that the peaks of ZnO became stronger and the full width at half maximum (FWHM) of the diffraction lines became narrower when the calcination temperature was 1200 °C. The mean crystallite sizes of the ZONH1-1200 particles estimated from the main XRD peaks based on the Scherer equation was calculated to be  $125 \pm 0.1$  nm.

TEM images and the EDX spectrum were examined in order to determine the morphology and size of ZONH1-1200. The TEM images and EDX spectrum of ZONH1-1200 are shown in Figure 7. The particles have an irregular shaped morphology and round shape morphology as well. The particle sizes of the round shapes are 100 nm while the size of the irregular shapes is 300 nm. The EDX spectrum clearly revealed that ZONH1-1200 has a zinc oxide structure (Cu and C signals from a TEM grid), which also indicates that Al, Fe and S are involved on the surface of ZnO nanoparticles.

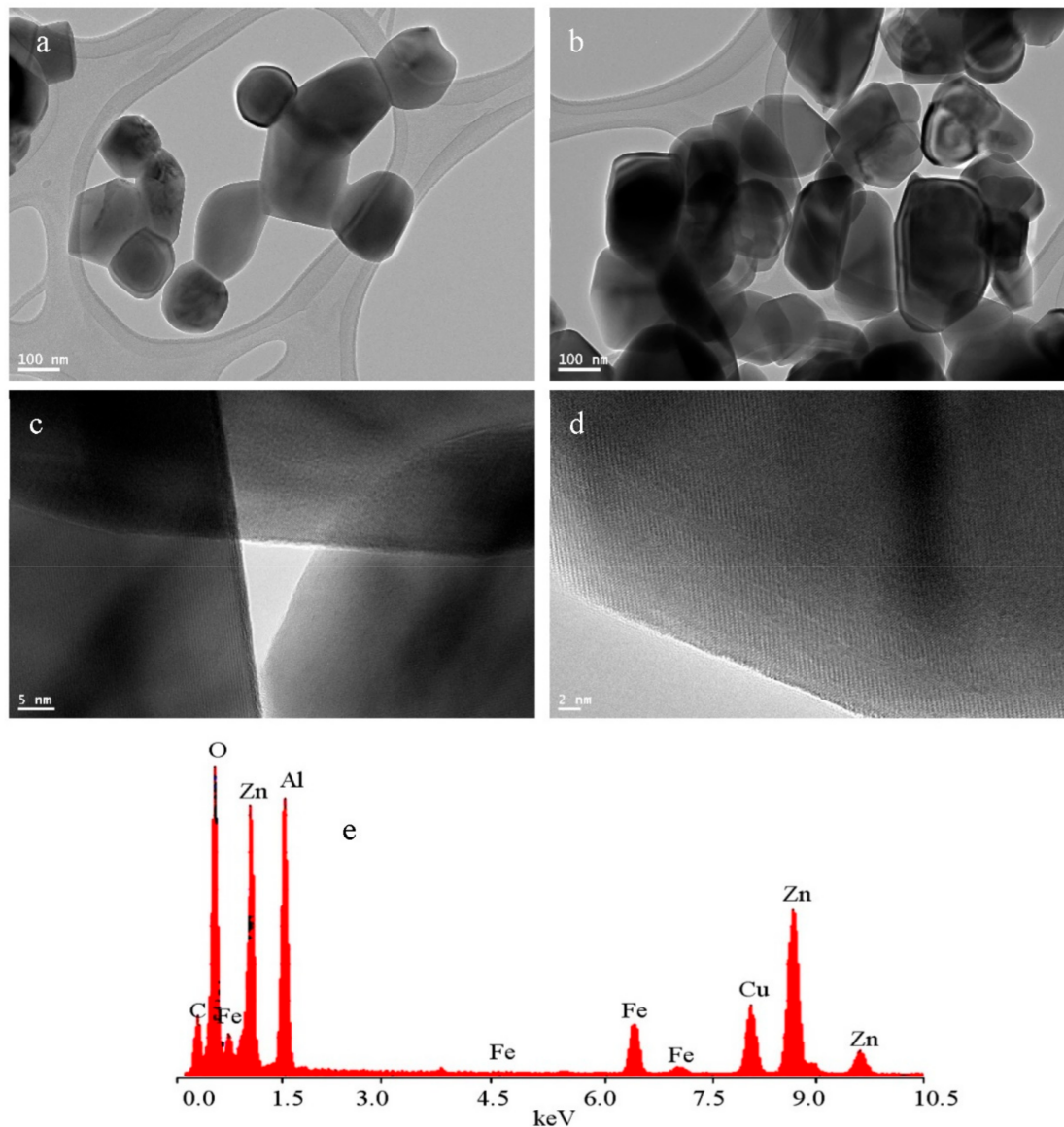


Figure 7. TEM images (a–d) and EDX spectrum (e) of the nanohybrid ZONH1-1200.

By the same technique, the Al-doped ZnO (AZO-500) was prepared without naphthol green B after thermal treatment at 500 °C. Also, the series of the multi-doped zinc oxide (ZONH2 and ZONH3) were produced using lower concentrations of naphthol green B and thermal treatment at 500 °C. By comparing with the standard entire diffraction pattern of zincite phase (JCPDS 79-205) and wurtzite (JCPDS 57-1451) ZnO crystal, XRD patterns showed that AZO-500, ZONH2-500 and ZONH3-500 have zinc oxide structures as shown in Figure 8. Also, Figure 8 indicates that the dopants are homogeneously dispersed in the matrix of ZnO because no peak observed for Al-species in all the calcined samples.

The characteristic peaks of zincite phase observed in the XRD pattern of the sample AZO-500 were broad and diffuse, Figure 8a, possibly because of the involvement of the amorphous structure of aluminum oxide inside the zincite phase. For the samples ZONH2-500 and ZONH3-500, the peaks of zinc oxide became clearer agreeing with the main sample ZONH1-500. SEM images showed that the samples ZONH-2 and ZONH-3 have nanoplates. These nanoplates have a self-assembly behavior to build flower-like structures as shown in Figure 9.

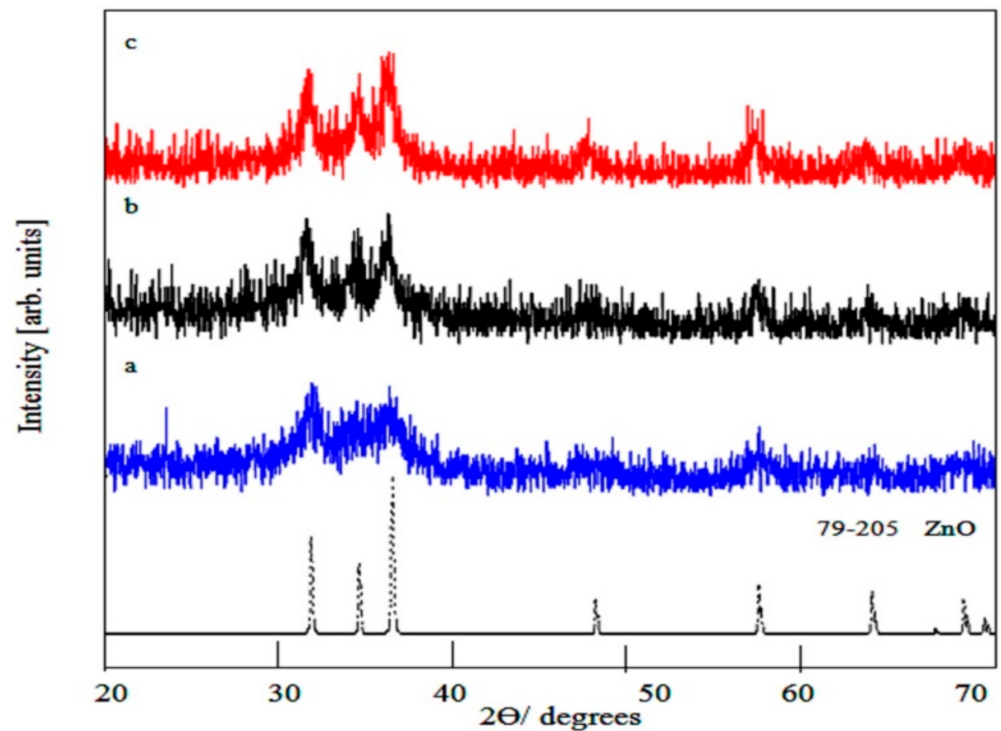


Figure 8. X-ray diffraction patterns of: (a) AZO-500, (b) ZONH2-500 and (c) ZONH3-500.

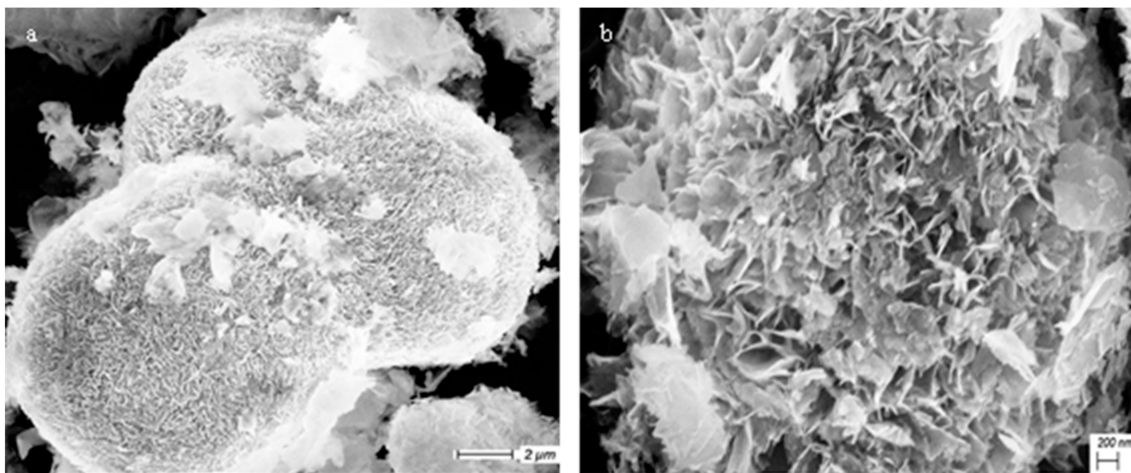
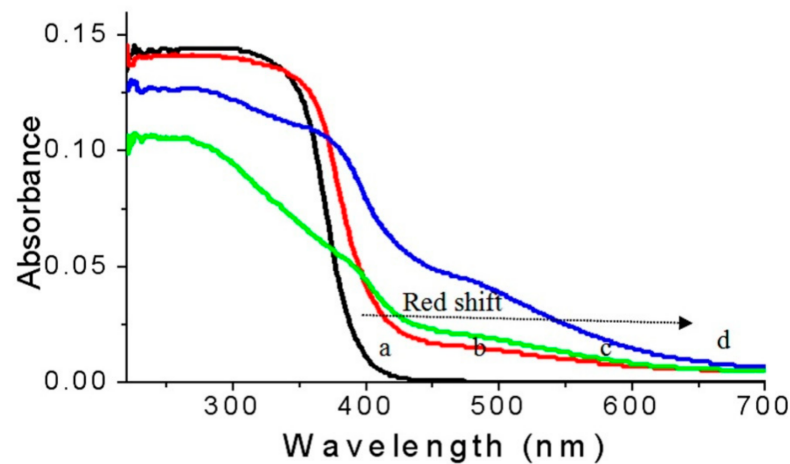


Figure 9. Scanning electron microscope (SEM) images of: (a) ZONH2-500 and (b) ZONH3-500.

### 3.3. Optical Properties

In order to avoid the difficulties introduced by particle size or the physical state of the samples, the optical parameters were measured by UV–VIS–NIR diffuse reflectance technique [47].

This technique is considered a powerful tool for recording the UV-vis absorption spectra of the powder samples and providing important information about the band gap energy of the prepared nanomaterials. In case of the sample AZO-500, Figure 10a showed that the Al-doped zinc oxide which was prepared without green dyes, did not have obvious absorption in the range of visible region (400–800 nm) indicating that it is inactive with illumination of sunlight. At the same time, a strong UV absorption peak was observed beneath 400 nm which could be ascribed to the transition of electrons from the oxygen 2p level to the metal 4s or 4p level [48].



**Figure 10.** Ultraviolet–visible (UV-Vis) spectra of (a) AZO-500, (b) ZONH2-500, (c) ZONH3-500 and (d) ZONH1-500.

The nature and the value of the optical band gap energy ( $E_g$ ) of the prepared samples can be calculated from the electronic excitation from the valence band to the conduction band. The fundamental formula which connects the incident photon energy ( $h\nu$ ) and the absorption coefficient ( $\alpha$ ) can be observed in the following equation [42]:

$$(\alpha h\nu)^m = A(h\nu - E_g) \quad (1)$$

where the value  $m$  depends on the optical absorption process and the constant  $A$  characterizes the transition probability. According to the electronic transitions, the theoretical value of ( $m$ ) is equivalent to 2 or  $\frac{1}{2}$  for direct allowed or indirect allowed, respectively.

The electronic transition of AZO-500 is a direct process from the oxygen 2p to the metal ns or np levels ( $n = 4$  for Zn and  $n = 3$  for Al) [49]. Thus, the band gap energy of AZO can be obtained by plotting  $(\alpha h\nu)^2$  and  $(h\nu)$  and the straight line range of these plots can be extended to the  $(h\nu)$  axis to obtain the values of optical band gap of the samples at  $(\alpha h\nu)^2 = 0$ .

The band gap energy ( $E_g$ ) value of AZO-500 at room temperature is  $3.25 \pm 0.01$  eV as shown in Figure 11a and Table 2. It is different from that of  $\text{Al}_2\text{O}_3$  ( $E_g = 3.60$  eV). By comparing with the ZnO ( $E_g = 3.30$  eV), the band gap energy of the Al-doped ZnO was a slightly lower because of the dopant centers in the matrix of zinc oxide [7].

**Table 2.** Band gap energy calculated from the results of the UV-Vis spectra.

Scheme	Band Gap Energy (eV)
AZO-500	$3.25 \pm 0.01$
ZONH2-500	$3.15 \pm 0.01$
ZONH3-500	$3.05 \pm 0.01$
ZONH1-500	$2.80 \pm 0.01$

By a multi-doping process through green dyes, the optical properties of the multi-doped zinc oxides were gradually improved as shown in Figures 10 and 11 and noticed in Table 2. Figure 10b showed shifting for the absorption edge of ZONH2-500 toward 600 nm leading to wider spectrum than that of AZO-500. At the same time, the maximum intensity of the absorbance of ZONH2-500 was observed to  $350 \pm 10$  nm. Also, the band gap energy of ZONH2-500 decreased to become  $3.15 \pm 0.01$  eV as seen in Figure 11b and Table 2. These results indicated that the first dose of multi-doping process started to improve the optical properties ZnO to be active in sunlight.

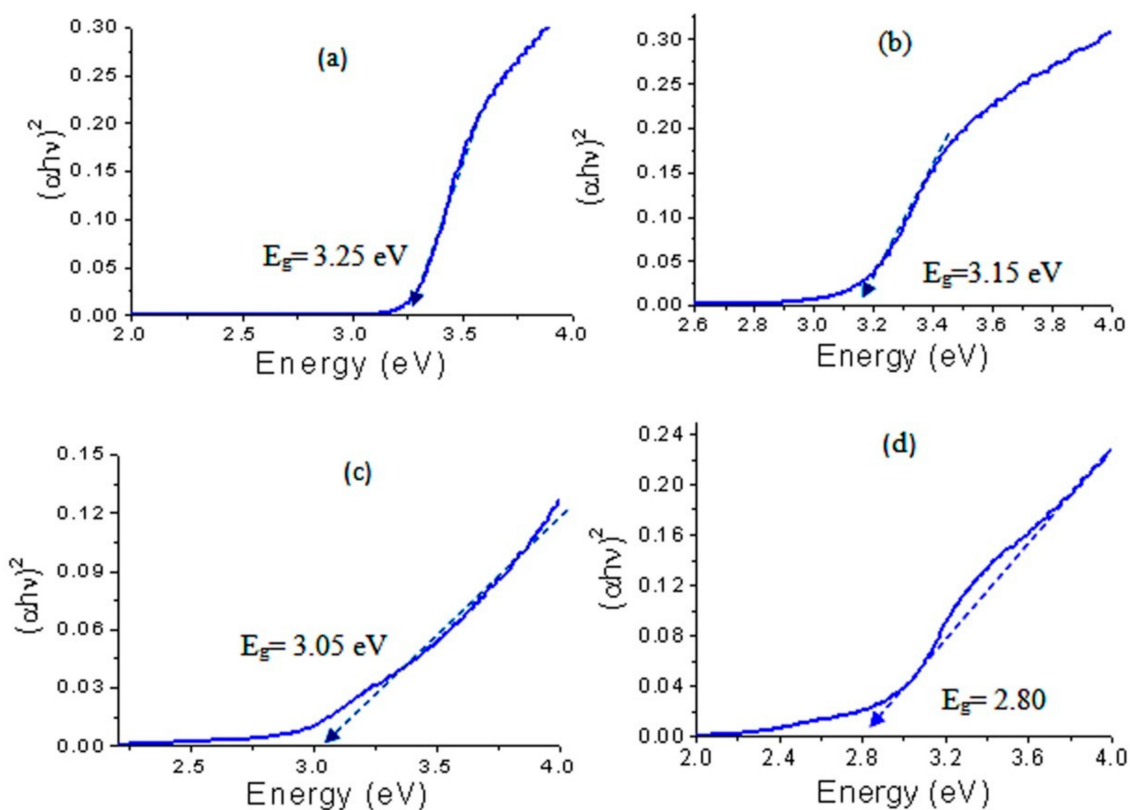


Figure 11. Band gap energy of (a) AZO-500, (b) ZONH2-500, (c) ZONH3-500 and (d) ZONH1-500.

In case of the second sample ZONH3-500, Figure 10c revealed that the absorbance spectrum became wider. The absorbance edge expanded to cover the wavelengths from 200 nm to 650 nm. This wide range of absorbance suggests that ZONH3-500 may be effective in sunlight. By calculating the band gap energy of ZONH3-500, this speculation was confirmed through reduction of the band gap to be  $3.00 \pm 0.01$  eV as shown in Figure 11c and Table 2.

These observations became clearer in the third sample ZONH1-500 as shown in Figure 10d. By increasing the percentage of the dopants, Figure 10d showed wider absorbance for ZONH1-500 with shifting the absorbance edge to higher wavelength. The band gap energy of ZONH1-500 decreased to be  $2.80 \pm 0.01$  eV as shown in Figure 11d and Table 2. The low band gap energy indicates that the third sample may be optically active in sunlight. By comparing with the band gap energy of the sample AZO-500, band gap narrowing of zinc oxide was observed by multi-doping process and this narrowing is gradually increased by increasing the content of green dyes. This band gap energy narrowing can be clarified according to creating new levels in the band gap region by the defect states of the dopants. This speculation was supported by observing the gradual reduction of band gap energy with increasing the contents of dopants inside the matrix of zinc oxide.

According to these results, the samples of the multi-doped zinc oxides may be active in sunlight. Therefore, these samples were tested in sunlight and studied for photocatalytic degradation of industrial pollutants as shown below.

### 3.4. Effective Removal of Pollutants

To determine the photo activity of the multi-doped zinc oxides in the visible light, the photocatalytic degradation of the industrial pollutants (Naphthol Green B dyes; NGB) was investigated in the presence of water and one of the prepared samples ZONH2-500, ZONH3-500 or ZONH1-500 using sunlight as shown in Figure 12. In addition, the sample AZO-500 has used the same process for comparing with the photo activity of the multi-

doped samples. In a blank experiment, a high stability was observed for the NGB in sunlight because the concentration of the green dyes did not change in sunlight.

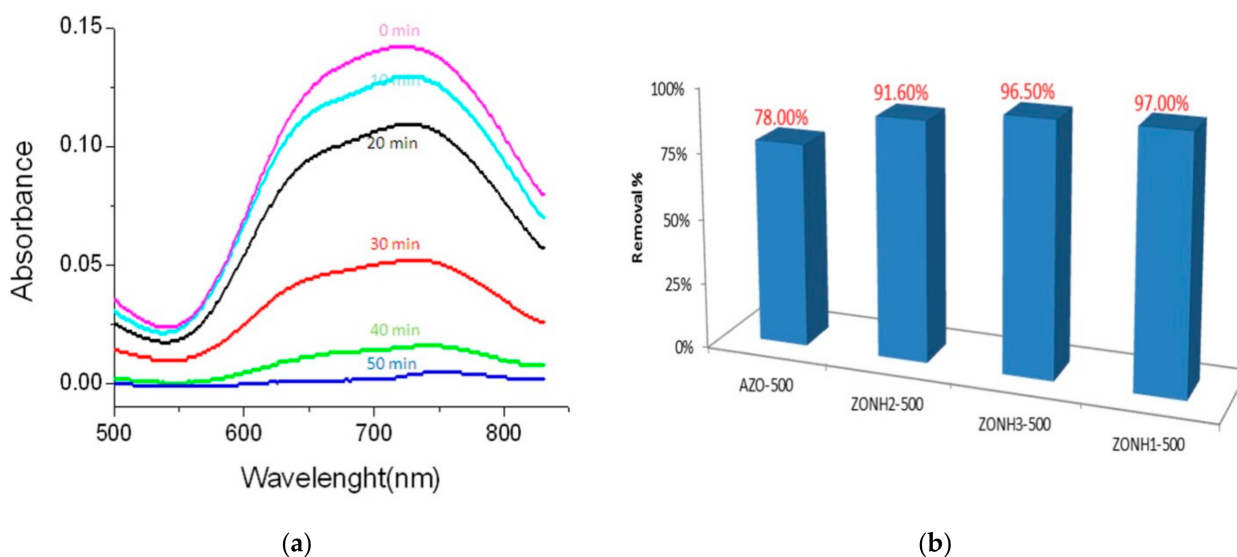


**Figure 12.** (a) Absorbance spectra of Naphthol Green B after 50 min in sunlight using ZONH1-500 and (b) photocatalytic removal of Naphthol Green B in the presence of sunlight and the different prepared nanomaterials.

The absorbance of the green solution of Naphthol Green B was measured to determine the concentration of the green dyes after interval times. Figure 12a shows that the photocatalytic degradation of NGB in the presence of the sample ZONH1-500 increased with increasing the irradiation time in sunlight. The complete removal and decolorization of the NGB were approximately accomplished after 50 min of sunlight irradiation as seen in Figure 12a. Figure 12b shows that 97.00% of the green dyes were removed by ZONH1-500 after irradiating for 50 min in sunlight. In case of using the other multi-doped ZnO, the removal percentages were above 90.00% in the same period. Figure 12b indicates that ZONH2-500 and ZONH3-500 removed 91.60% and 96.50% of the pollutants after 50 min of sunlight irradiation. By comparing with the Al-doped ZnO (AZO-500), the samples of multi-doped ZnO were more effective for photocatalytic degradation of the pollutants in sunlight. Figure 12b shows that 78.00% of the pollutants disappeared after 50 min of sunlight irradiation by the sample AZO-500. Also, compared with the results of the Al-doped ZnO nanoparticles that previously published for our laboratory, the multi-doped ZnO was very effective in sunlight. The complete removal of NGB was achieved after 6 h illumination of sunlight [7]. Following the same trend, our recent published data for the aluminum zinc oxide nanocomposite-coated carbon nanotubes indicated that the complete decomposition and decolorization of green dye were attained after 1.25–1.30 h of irradiation of UV light [50]. This means that the multi-doping process was very effective for improving the photo activity of zinc oxide and the Al-doped zinc oxide through decreasing their band gap energy.

This finding was confirmed through the kinetic study of photocatalytic degradation of NGB for AZO-500, ZONH1-500, ZONH2-500 and ZONH3-500 by the following equation:

$$\ln(C_0/C) = kt \quad (2)$$

where the absorbance of NGB at different times is  $C$ , the absorbance of NGB at  $t = 0$  is  $C_0$  and the process rate constant is  $k$ . Figure 13 shows the kinetic study of the photocatalytic degradation of NGB using the different prepared materials in the presence of sunlight through the plots of  $\ln(C_0/C)$  versus the irradiation time of sunlight.

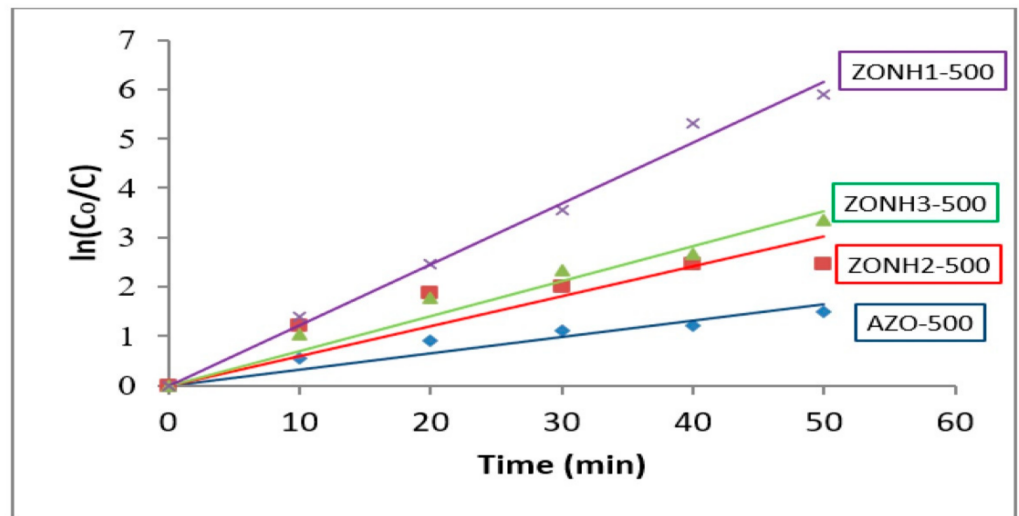


**Figure 13.** Kinetic study of the photocatalytic removal of Naphthol Green B in presence of sunlight and the different prepared nanomaterials.

From Figure 13, it could be inferred that the decolorization and the photocatalytic degradation of NGB by sunlight employing AZO-500 as a photocatalyst exhibited pseudo-first-order kinetic with rate constant  $0.03 \text{ min}^{-1}$ . By using the multi-doped zinc oxides samples, the rate constant of ZONH2-500 and ZONH3-500 increased to become two times higher than that of AZO-500. Figure 13 shows that the rates constant of the reaction using the samples ZONH2-500 and ZONH3-500 were  $0.06 \text{ min}^{-1}$  and  $0.07 \text{ min}^{-1}$ . In the case of using ZONH1-500, the rate constant increased to become  $0.12 \text{ min}^{-1}$ . This means that the rate of the reaction in presence of the multi-doped ZnO was four times faster than that using the Al-doped ZnO.

#### 4. Discussion

In order to obtain unusual optical properties for zinc oxide which cannot be attained by conventional reactions, host–guest interaction has been used to prepare an almost unlimited set of new compounds (organic–inorganic nanohybrids) with a large spectrum of known or unknown properties [51,52]. By this technique, zinc oxide was doped by Al, Fe, N, S and colored organic species through intercalation and confinement of Naphthol Green B inside two-dimensional layered structures.

The Zn-Al two-dimensional layered structure confines green dye that acts as a guest and is a source for different metals and non-metals in only one dimension. The molecules of green dyes are confined between two hard layers producing nanohybrids. The interlayered spacing of the nanolayered structures increased and expanded depending on the thickness of a guest species as shown in Figure 14.

By thermal treatment at  $500 \text{ }^\circ\text{C}$ , the incorporation of inorganic particles such as Al, Fe, N and S with ZnO structure was achieved in the nano scale after decomposing the intercalated organic species. Also, it is an efficient way for a homogeneous dispersion of inorganic elements inside the structure of zinc oxide improving its optical properties. Also, the decomposition of organic species and production of a large amount of  $\text{CO}_2$  inside the interlayered spacing of the nanohybrids led to the formation of nanofibers because the lamellae produced by exfoliation of layered solids and having thickness of  $0.48 \text{ nm}$  decomposed under the effect of the inner high pressure of the evolved gases from the decomposition of green dye.

In this way, a series of the multi-doped zinc oxides was produced and they showed high performance as photocatalysts in sunlight. This high performance in the field of photocatalytic degradation of industrial pollutants could be explained by the reduction of band gap energy of zinc oxide from  $3.30 \pm 0.01 \text{ eV}$  to  $2.80 \pm 0.01 \text{ eV}$  [53].

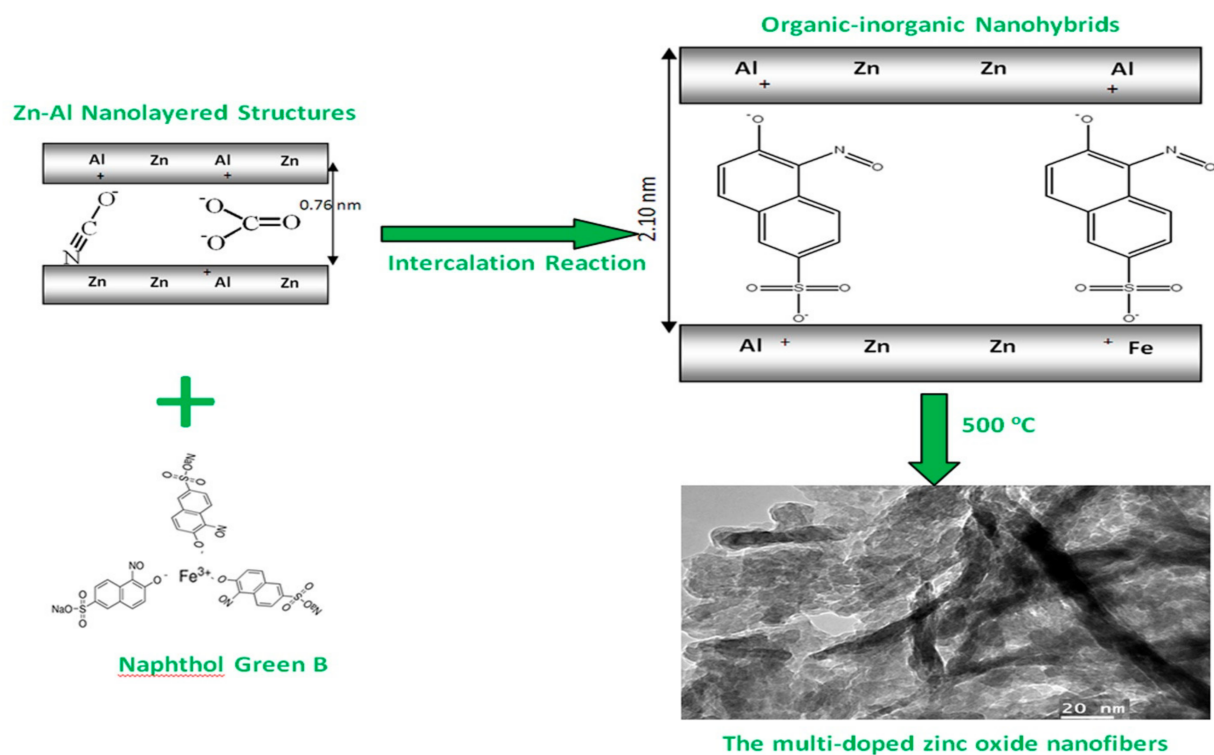
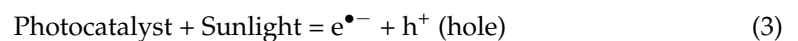


**Figure 14.** Schematic representation for multi-doping process for zinc oxide.

In our previous study [7], the Al-doped zinc oxide, which had band gap energy of  $3.23 \pm 0.01$  eV, showed complete degradation of Naphthol Green B after 6 h of irradiation of sunlight because of the small narrowing for the band gap energy from  $3.30 \pm 0.01$  eV to  $3.23 \pm 0.01$  eV.

In the current study, the multi-doped zinc oxide showed a complete degradation of the green dyes after 50 min because of the strong narrowing band gap energy of  $2.80 \pm 0.01$  eV. This means that the doping by one metal (Al) showed a little effect for the band gap energy while the multi-doping process led to significant effects on the band gap energy. According to many body effects of dopants on the conduction and the valence bands, band gap narrowing was observed. Therefore, for the multi-doping process, band gap narrowing became large. Many body effects such as exchange energy due to electron–electron and electron–impurity interactions produced by the presence of dopants caused a red shift of band gap and affected the optical absorption edge of zinc oxide [7].

In the case of the normal effect of a photocatalyst [54], the photocatalytic processes depend on the excitation reaction of photo-active material (3):



According to the quality of the photocatalyst, the electrons in the valence band acquired enough energy (the photons of energy equal to, or higher than its band gap energy) to be excited and jump to the conduction band. At the same time, holes were produced in the valence band as shown in process (3). These electron-hole pairs produced strong oxidizing agents [55]. For the multi-doped zinc oxide, the low band gap energy led to accelerating the excitation reaction in sunlight. Accordingly, a large number of oxidizing agents was produced and destroyed the pollutants in a short time.

## 5. Conclusions

The current study has many objectives in the field of development of optical materials. The first objective focused on the production of advanced structures of zinc oxide nanofibers and nanoplates through non-conventional technique. These advanced structures were

produced through doping zinc oxide with aluminum, iron, nitrogen and sulfur in addition to organic dyes through a one-step process. The second objective was conversion of zinc oxide to act as effective photocatalysts in sunlight. It was achieved by narrowing its band gap energy from  $3.30 \pm 0.01$  eV to  $2.80 \pm 0.01$  eV. Fast photocatalytic degradation of industrial pollutants was the third objective which was accomplished through accelerating the photocatalytic removal of green dyes from water using the multi-doped zinc oxide. By comparing with the Al-doped ZnO, the reaction rate of the photocatalytic removal of green dyes from water was four times faster in the case of using the multi-doped ZnO.

We concluded that many objectives such as a doping process with different transition elements with homogeneous dispersion, morphological changes, nanomaterials formation, and the introduction of surface defects could be achieved through a one-step process depending on host–guest interactions. By host–guest interaction, organic–inorganic nanohybrids were formed in order arrangements through nanolayered structures. This strategy allows combining different metals and non-metals with zinc oxide in special arrangements in the nano scale and producing advanced nanostructures. These advanced nanostructures of zinc oxide led to increase its ability to suppress charges of recombination, narrowing its band gap energy and producing effective photocatalysts in sunlight.

**Author Contributions:** Conceptualization, O.S.; methodology, O.S.; formal analysis, N.M.S., F.A. and S.K.; Resources, O.S., N.M.S. and A.A.; Visualization, S.K. and F.A.; supervision, A.A.; project administration, O.S.; funding acquisition, O.S.; writing—original draft preparation, O.S.; writing—review and editing, F.A., S.K. and A.A. All authors have read and agreed to the published version of the manuscript.

**Funding:** This work was funded by the Deanship of Scientific Research at King Faisal University under Nasher Track (Grant No. 216055).

**Data Availability Statement:** Data is available based on reasonable request.

**Acknowledgments:** The authors acknowledge the Deanship of Scientific Research at King Faisal University for financial support under Nasher Track (Grant No. 216055).

**Conflicts of Interest:** The authors declare no conflict of interest.

## References

1. Nasr, M.; Eid, C.; Habchi, R.; Miele, P.; Bechelany, M. Recent progress on titanium dioxide nanomaterials for photocatalytic applications. *ChemSusChem* **2018**, *11*, 3023–3047. [[CrossRef](#)] [[PubMed](#)]
2. Alshoaibi, A.; Saber, O.; Ahmed, F. Enhancement of optical activity and properties of barium titanium oxides to be active in sunlight through using hollandite phase instead of perovskite phase. *Crystals* **2021**, *11*, 550. [[CrossRef](#)]
3. Saber, O.; Alshoaibi, A.; Al-Yaari, M.; Osama, M. Conversion of non-optical material to photo-active, nanocomposites through non-conventional techniques for water purification by solar energy. *Molecules* **2020**, *25*, 4484. [[CrossRef](#)] [[PubMed](#)]
4. Dindar, B.; Icli, S. Unusual photoreactivity of ZnO under concentrated sun light. *J. Photochem. Photobiol. A Chem.* **2001**, *140*, 263–268. [[CrossRef](#)]
5. Yeber, M.C.; Roderiguez, J.; Freer, J.; Baeza, J.; Duran, N.; Mansilla, H.D. Advanced oxidation of a pulp mill bleaching wastewater. *Chemosphere* **1999**, *39*, 1679–1688. [[CrossRef](#)]
6. Behnajady, M.A.; Modirshahla, N.; Hamzavi, R. Kinetic study on photocatalytic degradation of C.I. Acid Yellow 23 by ZnO photocatalyst. *J. Hazard. Mater. B* **2006**, *133*, 226–232. [[CrossRef](#)] [[PubMed](#)]
7. Saber, O.; El-Brollosy, T.; AlJaafari, A. Improvement of photocatalytic degradation of naphthol green B under solar light using aluminum doping of zinc oxide nanoparticles. *Water Air Soil Pollut.* **2012**, *223*, 4615–4626. [[CrossRef](#)]
8. Gupta, V.K.; Jain, R.; Nayak, A.; Agarwal, S.; Shrivastava, M. Removal of the hazardous dye—Tartrazine by photodegradation on titanium dioxide surface. *Mater. Sci. Eng. C* **2011**, *31*, 1062–1067. [[CrossRef](#)]
9. Sakthivel, S.; Kish, H. Photocatalytic and photoelectrochemical properties of N-doped titanium dioxide. *ChemPhysChem* **2003**, *4*, 487–490. [[CrossRef](#)] [[PubMed](#)]
10. Sun, J.H.; Dong, S.Y.; Wang, Y.K.; Sun, S.P. Preparation and photocatalytic property of a novel dumbbell-shaped ZnO microcrystal photocatalyst. *J. Hazard. Mater.* **2009**, *172*, 1520–1526. [[CrossRef](#)]
11. Wang, Q.; Tang, C.; Jiang, C.; Du, D.; Wang, F.; Song, J. Role of Substrate Roughness in ZnO Nanowire Arrays Growth by Hydrothermal Approach. *Acta Metall. Sin. Engl. Lett.* **2016**, *29*, 237–242. [[CrossRef](#)]
12. Zhou, W.; Li, X.; Qin, L.; Kang, S. Facile Preparation of Ag<sub>2</sub>ZnGeO<sub>4</sub> Flower-like Hierarchical Nanostructure and Its Photocatalytic Activity. *J. Mater. Sci. Technol.* **2017**, *33*, 47–51. [[CrossRef](#)]

13. Liu, C.; Xu, H.; Wang, L.; Qin, X. Facile One-Pot Green Synthesis and Antibacterial Activities of GO/Ag Nanocomposites. *Acta Metall. Sin. Engl. Lett.* **2017**, *30*, 36–44. [[CrossRef](#)]
14. Bai, X.; Wang, L.; Zong, R.; Lv, Y.; Sun, Y.; Zhu, Y. Performance enhancement of ZnO photocatalyst via synergic effect of surface oxygen defect and graphene hybridization. *Langmuir* **2013**, *29*, 3097–3105. [[CrossRef](#)] [[PubMed](#)]
15. Leung, Y.; Chen, X.; Ng, A.; Guo, M.; Liu, F.; Djuricic, A.; Chan, W.; Shi, X.; Van Hove, M. Green emission in ZnO nanostructures—Examination of the roles of oxygen and zinc vacancies. *Appl. Surf. Sci.* **2013**, *271*, 202–209. [[CrossRef](#)]
16. Wojnarowicz, J.; Chudoba, T.; Koltsov, I.; Gierlotka, S.; Dworakowska, S.; Lojkowski, W. Size control mechanism of ZnO nanoparticles obtained in microwave solvothermal synthesis. *Nanotechnology* **2019**, *29*, 06561. [[CrossRef](#)]
17. Pimentel, A.; Ferreira, S.H.; Nunes, D.; Calmeiro, T.; Martins, R.; Fortunato, E. Microwave Synthesized ZnO Nanorod Arrays for UV Sensors: A Seed Layer Annealing Temperature Study. *Materials* **2016**, *9*, 299. [[CrossRef](#)]
18. Samadipakchin, P.; Mortaheb, H.R.; Zolfaghari, A. ZnO nanotubes: Preparation and photocatalytic performance evaluation. *J. Photochem. Photobiol. A Chem.* **2017**, *337*, 91. [[CrossRef](#)]
19. Zhang, Y.; Ram, M.K.; Stefanakos, E.K.; Goswami, Y.D. Synthesis, Characterization, and Applications of ZnO Nanowires. *J. Nanomater.* **2012**, *12*, 624520. [[CrossRef](#)]
20. Diguna, L.J.; Fitriani, A.D.; Liasari, B.R.; Timuda, G.E.; Widayatno, W.B.; Wismogroho, A.S.; Zeng, S.; Birowosuto, M.D.; Amal, M.I. Optical and Photodetection Properties of ZnO Nanoparticles Recovered from Zn Dross. *Crystals* **2021**, *11*, 6. [[CrossRef](#)]
21. Chen, H.; Zhao, L.; He, X.; Wang, G.; Wang, X.; Fang, W.; Du, X. In situ Formed Fan-Shaped Nanowires in Biomorphic SiO<sub>2</sub>: A Multidimensional Composite of Hierarchical Porous Material and Organic Pollutant Adsorption Behavior. *Acta Metall. Sin. Engl. Lett.* **2017**, *30*, 104–112. [[CrossRef](#)]
22. Zhong, J.B.; Li, J.Z.; He, X.Y.; Zeng, J.; Lu, Y.; Hu, W.; Lin, K. Improved Photocatalytic Performance of Pd-Doped ZnO. *Curr. Appl. Phys.* **2012**, *12*, 998–1001. [[CrossRef](#)]
23. Sin, J.; Lam, S.; Lee, K.; Mohamed, A. Preparation and photocatalytic properties of visible light-driven samarium-doped ZnO nanorods. *Ceram. Int.* **2013**, *39*, 5833–5843. [[CrossRef](#)]
24. Ahmad, M.; Ahmed, E.; Zhang, Y.; Khalid, N.R.; Xu, J.; Ullah, M.; Hong, Z. Preparation of Highly Efficient Al-Doped ZnO Photocatalyst by Combustion Synthesis. *Curr. Appl. Phys.* **2013**, *13*, 697–704. [[CrossRef](#)]
25. Huang, L.; Ren, N.; Li, B.; Zhou, M. Effect of Annealing on the Morphology, Structure and Photoelectric Properties of AZO/Pt/FTO Trilayer Films. *Acta Metall. Sin. Engl. Lett.* **2015**, *28*, 281–288. [[CrossRef](#)]
26. Haja sheriff, M.H.; Murugan, S.; Manivasaham, A.; Ashok Kumar, R. Electro spray technique to enhance the physical property of Sulphur doped zinc oxide thin film. *Mater. Today Proc.* **2021**, *47*, 1717–1723. [[CrossRef](#)]
27. Riaz, A.; Ashraf, A.; Taimoor, H.; Javed, S.; Akram, M.A.; Islam, M.; Mujahid, M.; Ahmad, I.; Saeed, K. Photocatalytic and Photostability Behavior of Ag- and/or Al- Doped ZnO Films in Methylene Blue and Rhodamine B Under UV-C Irradiation. *Coatings* **2019**, *9*, 202. [[CrossRef](#)]
28. Lavand, A.B.; Malghe, Y.S. Synthesis, characterization and visible light photocatalytic activity of nitrogen-doped zinc oxide nanospheres. *J. Asian Ceram. Soc.* **2018**, *3*, 305–310. [[CrossRef](#)]
29. Hamrouni, S.; AlKhalifah, M.S.; El-Bana, M.S.; Zobaidi, S.K.; Belgacem, S. Deposition and characterization of spin-coated n-type ZnO thin film for potential window layer of solar cell. *Appl. Phys. A* **2018**, *124*, 555. [[CrossRef](#)]
30. Farrag, A.A.-G.; Balboul, M.R. Nano ZnO thin films synthesis by sol-gel spin coating method as a transparent layer for solar cell applications. *J. Sol-Gel Sci. Technol.* **2016**, *82*, 269–279. [[CrossRef](#)]
31. Yan, X.; Venkataraj, S.; Aberle, A.G. Wet-Chemical Surface Texturing of Sputter-Deposited ZnO: Al Films as Front Electrode for Thin-Film Silicon Solar Cells. *Int. J. Photoenergy* **2015**, *2015*, 1–10. [[CrossRef](#)]
32. Islam, M.R.; Rahman, M.; Farhad, S.F.U.; Podder, J. Structural, optical and photocatalysis properties of sol-gel deposited Al-doped ZnO thin films. *Surf. Interfaces* **2019**, *16*, 120–126. [[CrossRef](#)]
33. Mahdavi, R.; Talesh, S.S.A. Sol-gel synthesis, structural and enhanced photocatalytic performance of Al doped ZnO nanoparticles. *Adv. Powder Technol.* **2017**, *28*, 1418–1425. [[CrossRef](#)]
34. Aydın, C.; AbdEl-sadek, M.S.; Zheng, K.; Yahia, I.S.; Yakuphanoglu, F. Synthesis, diffused reflectance and electrical properties of nanocrystalline Fe-doped ZnO via sol-gel calcination technique. *Opt. Laser Technol.* **2013**, *48*, 447–452. [[CrossRef](#)]
35. Ravichandran, K.; Sindhuja, E.; Uma, R.; Arun, T. Photocatalytic efficacy of ZnO films light intensity and thickness effects. *Surf. Eng.* **2017**, *33*, 512–520. [[CrossRef](#)]
36. Saber, O.; Asiri, S.M.; Ezzeldin, M.F.; El-Azab, W.I.M.; Abu-Abdeen, M. Designing Dual-Effect Nanohybrids for Removing Heavy Metals and Different Kinds of Anions from the Natural Water. *Materials* **2020**, *13*, 2524. [[CrossRef](#)]
37. Saber, O.; Aljaafari, A.; Osama, A.; Alshoabi, A. Optimization Conditions for Crystal Growth of Novel Nanolayers, Nanohybrids and Nanocomposites Based on Cobalt, Zirconium, Titanium and Silicon. *Chem. Sel.* **2019**, *4*, 580–588.
38. Faramawy, S.; Zaki, T.; Sakr, A.A.-E.; Saber, O.; Aboul-Gheit, A.K.; Hassan, S.A. The activity of Mg-Al layered double hydroxides intercalated with nitrogen containing anions towards the removal of carbon dioxide from natural gas. *J. Nat. Gas Sci. Eng.* **2018**, *54*, 72–82. [[CrossRef](#)]
39. Low, J.; Yu, J.; Jaroniec, M.; Wageh, S.; Al-Ghamdi, A.A. Heterojunction Photocatalysts. *Adv. Mater.* **2017**, *29*, 1601694. [[CrossRef](#)]
40. Amaro-Ortiz, A.; Yan, B.; D’Orazio, J.A. Ultraviolet Radiation, Aging and the Skin: Prevention of Damage by Topical cAMP Manipulation. *Molecules* **2014**, *19*, 6202–6219. [[CrossRef](#)]

41. Nakamoto, N. *Infrared and Raman Spectra of Inorganic and Coordination Compounds*, 4th ed.; Wiley: New York, NY, USA, 1986; pp. 121–139.
42. Saber, O.; Aljaafari, A.; Alomair, H.A.; Alshoaibi, A. Novel strategy for producing nanoplatelets to be used as building blocks for shaping nanofibers through layered double hydroxides and poly vinyl alcohol. *Chem. Sel.* **2019**, *4*, 4293–4300. [[CrossRef](#)]
43. Tang, Z.K.; Wong, G.K.L.; Yu, P.; Kawasaki, M.; Ohtomo, A.; Koinuma, H.; Segawa, Y. Room-temperature ultraviolet laser emission from self-assembled ZnO microcrystallite thin films. *Appl. Phys. Lett.* **1998**, *72*, 3270. [[CrossRef](#)]
44. van Dijken, A.; Makkinje, J.; Meijerink, A. The influence of particle size on the luminescence quantum efficiency of nanocrystalline ZnO particles. *J. Lumin.* **2001**, *92*, 323–328. [[CrossRef](#)]
45. Kind, H.; Yan, H.; Messer, B.; Law, M.; Yang, P. Nanowire Ultraviolet Photodetectors and Optical Switches. *Adv. Mater.* **2002**, *14*, 158–160. [[CrossRef](#)]
46. Nakrela, A.; Benramdane, N.; Bouzidi, A.; Kebbab, Z.; Medles, M.; Mathieu, C. Site location of Al-dopant in ZnO lattice by exploiting the structural and optical characterisation of ZnO:Al thin films. *Results Phys.* **2016**, *6*, 133–138. [[CrossRef](#)]
47. Barton, D.G.; Shtein, M.; Wilson, R.D.; Soled, S.L.; Iglesia, E. Structure and electronic properties of solid acids based on tungsten oxide nanostructures. *J. Phys. Chem. B* **1999**, *103*, 630–640. [[CrossRef](#)]
48. Ahmed, N.; Shibata, Y.; Taniguchi, T.; Izumi, Y. Photocatalytic conversion of carbon dioxide into methanol using zinc–copper–M(III) (M = aluminum, gallium) layered double hydroxides. *J. Catal.* **2011**, *279*, 123–135. [[CrossRef](#)]
49. Pankove, J.I. *Optical Processes in Semiconductor*; Prentice-Hall: Englewood Cliffs, NJ, USA, 1971; pp. 1–72.
50. Saber, O.; Alomair, H.; Abu-Abdeen, M.; Aljaafari, A. Fast Degradation of Green Pollutants Through Nanonets and Nanofibers of the Al-Doped Zinc Oxide. *Acta Metall. Sin. Engl. Lett.* **2018**, *31*, 533–546. [[CrossRef](#)]
51. Liang, C.; Zhang, X.; Wang, Z.; Wang, W.; Yang, M.; Dong, X. Organic/inorganic nanohybrids rejuvenate photodynamic cancer therapy. *J. Mater. Chem. B* **2020**, *8*, 4748–4763. [[CrossRef](#)]
52. Xu, J.W.; Cui, Z.M.; Liu, Z.Q.; Xu, F.; Chen, Y.S.; Luo, Y.L. Organic–Inorganic Nanohybrid Electrochemical Sensors from Multi-Walled Carbon Nanotubes Decorated with Zinc Oxide Nanoparticles and In-Situ Wrapped with Poly(2-methacryloyloxyethyl ferrocenecarboxylate) for Detection of the Content of Food Additives. *Nanomaterials* **2019**, *9*, 1388. [[CrossRef](#)]
53. Banerjee, T.; Podjaski, F.; Kröger, J.; Biswal, B.P.; Lotsch, B.V. Polymer photocatalysts for solar-to-chemical energy conversion. *Nat. Rev. Mater.* **2021**, *6*, 168–190. [[CrossRef](#)]
54. Zhou, H.; Qu, Y.; Zeida, T.; Duan, X. Towards highly efficient photocatalysts using semiconductor nanoarchitectures. *Energy Environ. Sci.* **2012**, *5*, 6732–6743. [[CrossRef](#)]
55. Kobayashi, A.; Muramatsu, E.; Yoshida, M.; Kato, M. Two Excited State Collaboration of Heteroleptic Ir(III)-Coumarin Complexes for H<sub>2</sub> Evolution Dye-Sensitized Photocatalysis. *Energies* **2021**, *14*, 2425. [[CrossRef](#)]